LBL-26057
Preprint

Lawrence Berkeley Laboratory
UNIVERSITY OF CALIFORNIA

EARTH SCIENCES DIVISION

Submitted to International Journal of Heat and Mass Transfer

A Similarity Solution for Two-Phase Fluid and Heat Flow Near High-Level Nuclear Waste Packages Emplaced in Porous Media

C. Doughty and K. Pruess

September 1988

Prepared for the U.S. Department of Energy under Contract Number DE-AC03-76SF00098.

DISCLAIMER

LBL-26057

A Similarity Solution for Two-Phase Fluid and Heat Flow near High-Level Nuclear Waste Packages Emplaced in Porous Media

Christine Doughty and Karsten Pruess

Earth Sciences Division
Lawrence Berkeley Laboratory
1 Cyclotron Road
Berkeley, California 94720

September 1988

This work was supported, in part, by the NNWSI Performance Assessment Division, Sandia National Laboratories, and the Director, Office of Energy Research, Office of Basic Energy Sciences, Division of Engineering and Geosciences, of the U.S. Department of Energy under Contract No. DE-AC03-76SF00098.

A Similarity Solution for Two-Phase Fluid and Heat Flow near High-Level Nuclear Waste Packages Emplaced in Porous Media

Christine Doughty and Karsten Pruess

Abstract

The emplacement of a heat source, such as a high-level nuclear waste package, into a geologic medium gives rise to strongly coupled thermal and hydrologic behavior. Under certain conditions, a heat pipe may develop, with significant impact on conditions at the heat source. In an infinite homogeneous permeable medium with a constant-strength linear heat source, the partial differential equations governing fluid and heat flows in a radial geometry can be converted to ordinary differential equations through the use of a similarity variable, $\eta = r/\sqrt{t}$. These equations are numerically integrated using an iterative "shooting" method to provide a description of temperature, pressure, saturation, heat flow, gas flow, and liquid flow conditions around a heat source such as a nuclear waste package. The similarity solution is verified by numerical finite-difference simulations. Illustrative solutions are given for a range of hydrologic and thermal parameters, and the likelihood of heat-pipe development for conditions at several proposed repository sites is discussed.

Nomenclature

M_e	energy accumulation term (J/m^3)
M_w, M_a	mass accumulation terms (kg/m^3)
c_r	rock specific heat (J/kg K)
C	volumetric heat capacity (J/m^3 K)
D_{va}	binary diffusion coefficient (m^2/s)
$\mathbf{F}$	discrepancy vector at upper limit of integration
h	enthalpy (J/kg)
K	Mobility (kg/s m Pa) ($K_j = kk_{rj}\rho_j/\mu_j$, $j = l, g$)
k	intrinsic permeability (m^2)
k_r	relative permeability
P	pressure (Pa)
P_c	capillary pressure (Pa) ($P_c = P_l - P_g$)
Q_e	heat flow rate (W/m)
Q_w, Q_a	mass flow rates (kg/s m) ($Q_m = Q_l^m + Q_g^m$, $m = w, a$)
$\tilde{Q}_e$	normalized heat flow rate (W/m) ($\tilde{Q}_e = Q_e/2\pi$)
$\tilde{Q}_w, \tilde{Q}_a$	normalized mass flow rates (kg/s m) ($\tilde{Q}_m = Q_m/2\pi$, $m = w, a$)
r	radial distance (m)
$\mathbf{R}$	matrix of partial derivatives for Newton-Raphson iteration
S	saturation
T	temperature (°C)
t	time (s)
u	internal energy (J/kg)
$\mathbf{V}$	vector of variables unspecified at lower limit of integration
X	mass fraction
z	integration variable ($z = \ln\eta$)
α_r	rock expansivity (K^{-1}) ($\alpha_r = (1/\phi)\partial\phi/\partial T$)
β_r	rock compressibility (Pa^{-1}) ($\beta_r = (1/\phi)\partial\phi/\partial P$)
β	ratio of kinematic viscosity for liquid- and gas-phase water
γ	desired accuracy of endpoints of numerical integration
δV_{Lj}	jth increment for Newton-Raphson iteration
ϵ	very small non-zero number
η	similarity variable ($\eta = r/\sqrt{t}$)
κ	thermal conductivity (W/m K)
λ	parameter in van Genuchten [19] characteristic curves
μ	dynamic viscosity (Pa s)
ρ	density (kg/m^3)
σ	vapor-liquid interfacial tension (N/m)
ϕ	porosity

Subscripts

a	air (also used as a superscript)
c	capillary, constant value
e	energy
g	gas phase
l	liquid phase
r	rock, residual, relative
sat	at saturation (vapor-liquid equilibrium)
w	water (also used as a superscript)
0	boundary condition, reference value
L	lower limit of integration
U	upper limit of integration

1. Introduction

The Nevada Nuclear Waste Site Investigations (NNWSI) project is investigating the feasibility of constructing a geologic repository for high-level nuclear waste at Yucca Mountain, Nevada, in a partially-saturated, highly-fractured volcanic formation. Several recent mathematical modeling studies [1, 2] have examined the thermohydrologic behavior surrounding a repository in this geologic setting. Undisturbed conditions are such that temperature is well below the saturation temperature, so water is primarily in the liquid phase, and the initial heat transfer from a waste package is mainly conductive. As temperatures around the repository increase to the saturation temperature, evaporation increases and vapor partial pressure becomes appreciable. Heat-pipe effects may contribute to or even dominate heat transfer in this regime. With time the heat pipe moves away from the waste packages, leaving a gas-phase zone in which heat transfer is again conduction-dominated. The conditions surrounding a waste package at some time after emplacement are shown schematically in Figure 1.

In the heat pipe region, heat transfer is primarily convective. Near the heat source liquid water vaporizes, causing pressurization of the gas phase and gas-phase flow away from the heat source. The water vapor condenses in cooler regions away from the heat source, depositing its latent heat of vaporization there. This sets up a saturation profile, with liquid saturation increasing away from the heat source. The saturation gradient drives the backflow of the liquid phase toward the heat source through capillary forces. The liquid then vaporizes again and repeats the cycle. This convective heat transfer is very efficient compared to conduction, so it occurs under nearly isothermal conditions.

The requirements for heat-pipe development are (1) the presence of a volatile fluid, which will boil when temperature reaches saturation temperature; and (2) a mechanism by which gas-phase fluid can flow away from the heat source and liquid-phase fluid toward it. Gas-phase flow occurs if medium permeability is sufficiently high, and the far-field pressure is lower than that at the heat source. Thus, heat-pipe behavior is

unlikely in deep water-saturated formations, where ambient pressure is much higher than open-hole or backfill pressure at the repository. Liquid flow requires sufficient mobility and capillary pressure. Mobility depends on liquid saturation as well as medium permeability, since below a certain residual saturation, liquid is immobile.

The present paper is concerned with an idealized version of the problem of fluid and heat flow near high-level nuclear waste packages. We study the behavior of an infinite homogeneous porous medium with uniform initial conditions, in response to the emplacement of an infinitely-long linear heat source of constant (time-independent) strength. Gravity effects are neglected, so that the system has a one-dimensional radial symmetry. With these simplifications, the coupled partial differential equations governing fluid and heat flow for radial geometry can be transformed into simpler ordinary differential equations through the use of a similarity variable, $\eta = r/\sqrt{t}$. This change of variable is known as the Boltzmann transformation in heat conduction problems. It has been applied to the thermohydrologic behavior of geologic media by O'Sullivan [3], who used it to analyze geothermal well-test data. Other researchers [4, 5] also have used the similarity concept for this purpose, but limited themselves to simplified thermodynamic relationships to allow quasi-analytic solutions.

Following O'Sullivan [3], we consider the fully non-linear problem with realistic thermodynamic relationships, which requires a numerical integration of the coupled differential equations. The main difference from O'Sullivan's treatment is that the mass flux boundary condition at $r = 0$, appropriate for geothermal production or injection wells, is here replaced by a heat flux boundary condition. Furthermore we include capillary pressure and heat conduction effects. These are unimportant for the geothermal well test problem, but are essential for the heat-driven problem considered here. Our general mathematical treatment includes two fluid components, water and air, although the specific solutions presented here are for water only.

Below, we describe the development of the governing equations and the techniques used for their integration. Next, the similarity solution is compared to results of numerical simulations, with excellent agreement. Finally, some characteristic features of thermohydrologic behavior in a geologic medium around a heat source are illustrated through application of the similarity solution.

2. Basic Equations

The governing equations for fluid and heat flow for a single-component system in radial geometry as given by O'Sullivan [3] consist of a mass balance for water and an energy balance

$$\frac{\partial M_w}{\partial t} + \frac{1}{2\pi r}\frac{\partial Q_w}{\partial r} = 0 \tag{1}$$

$$\frac{\partial M_e}{\partial t} + \frac{1}{2\pi r}\frac{\partial Q_e}{\partial r} = 0. \tag{2}$$

If air is present in the system, a mass balance for air is also needed

$$\frac{\partial M_a}{\partial t} + \frac{1}{2\pi r}\frac{\partial Q_a}{\partial r} = 0. \tag{3}$$

The subscripts w, a, and e refer to water, air, and energy, respectively. To simplify the notation, we introduce normalized flux terms, given by $\tilde{Q}=Q/2\pi$. With the rock and fluid assumed to be in local thermal equilibrium at all times, the accumulation terms are given by

$$M_m = \phi(S_l \rho_l X_l^m + S_g \rho_g X_g^m) \quad \text{for } m = w, a \tag{4}$$

$$M_e = (1-\phi)\rho_r c_r T + \phi(S_l \rho_l u_l + S_g \rho_g u_g) \tag{5}$$

where ϕ is porosity, S is saturation, ρ is density, X is mass fraction, c is specific heat, T is temperature, and u is internal energy. The subscripts l, g, and r refer to liquid phase, gas phase, and rock, respectively. The mass flow rate for each component, the sum of liquid and gas flow rates, is given by Darcy's Law, modified for two-phase flow. In the gas phase there is also a flow component due to binary diffusion

$$\tilde{Q}_m = \tilde{Q}_l^m + \tilde{Q}_g^m = \left[-\frac{k k_{rl} \rho_l X_l^m r}{\mu_l}\frac{\partial P_l}{\partial r}\right] + \left[-\frac{k k_{rg} \rho_g X_g^m r}{\mu_g}\frac{\partial P_g}{\partial r} - D_{va}\rho_g r \frac{\partial X_g^m}{\partial r}\right]$$

$$\text{for } m = w, a \tag{6}$$

where k is intrinsic permeability, k_{rj} is the relative permeability of phase j, μ is dynamic viscosity, P is pressure, and D_{va} is the diffusion coefficient for vapor-air mixtures. Liquid and gas pressures are related by the capillary pressure through $P_l = P_g + P_c$. If no air is present $X^w = 1$, $X^a = 0$, and the $m = a$ case of equations (4) and (6) is identically zero. The heat flow rate contains convective and conductive terms

$$\tilde{Q}_e = \sum_{\substack{j=l,g \\ m=w,a}} h_j^m \tilde{Q}_j^m - \kappa r \frac{\partial T}{\partial r} \tag{7}$$

where h is enthalpy and κ is thermal conductivity.

Equations (1), (2), (3), (6), and (7) make up a set of six coupled first-order partial differential equations for six unknowns (or primary variables). In single-phase regions S_g is constant, so $\tilde{Q}_w$, $\tilde{Q}_a$, $\tilde{Q}_e$, P_g, X_g^a, and T may be taken as the primary variables. In two-phase regions T depends on P_g and X through the saturation curve, so $\tilde{Q}_w$, $\tilde{Q}_a$, $\tilde{Q}_e$, P_g, X_g^a, and S_g become the primary variables. All other thermophysical properties can be expressed as functions of the primary variables, as described in Appendix A.

Note that by substituting equations (6) and (7) into equations (1), (2), and (3) we could obtain a set of three second-order differential equations for three unknowns: P_g, X_g^a, and T in single-phase regions, and P_g, X_g^a, and S_g in two-phase regions. While this set of equations may seem simpler than a set of six first-order equations, for numerical integration purposes it is preferable to treat first-order equations.

The uniform initial conditions are given by $\tilde{Q}_w = \tilde{Q}_a = \tilde{Q}_e = 0$, $P_g = P_0$, $X_g^a = X_0$, and $S_g = S_0$ for all r. The boundary conditions as $r \to 0$ are no mass flow ($\tilde{Q}_w = 0$, $\tilde{Q}_a = 0$) and constant heat flow ($\tilde{Q}_e = Q_{e0}/2\pi \equiv \tilde{Q}_{e0}$, where Q_{e0} is the heat source strength per unit length). The boundary conditions as $r \to \infty$ are unchanged from the initial values: $P_g = P_0$, $X_g^a = X_0$, and $S_g = S_0$.

Following O'Sullivan [3] we introduce a similarity variable $\eta = r/\sqrt{t}$ and rewrite the governing equations as

$$-\frac{\eta^2}{2}\frac{dM_m}{d\eta}+\frac{d\tilde{Q}_m}{d\eta}=0 \quad \text{for } m=w,a \tag{8}$$

$$-\frac{\eta^2}{2}\frac{dM_e}{d\eta}+\frac{d\tilde{Q}_e}{d\eta}=0 \tag{9}$$

$$\tilde{Q}_m=\left[-K_l X_l^m \eta\frac{dP_l}{d\eta}\right]+\left[-K_g X_g^m \eta\frac{dP_g}{d\eta}-D_{va}\rho_g\eta\frac{dX_g^m}{d\eta}\right] \quad \text{for } m=w,a \tag{10}$$

$$\tilde{Q}_e=\sum_{\substack{j=l,g\\ m=w,a}} h_j^m \tilde{Q}_j^m-\kappa\eta\frac{dT}{d\eta} \tag{11}$$

where liquid and gas phase mobilities have been defined as $K_l \equiv kk_{rl}\rho_l/\mu_l$ and $K_g \equiv kk_{rg}\rho_g/\mu_g$. Together the initial and boundary conditions become boundary conditions given by

$$\tilde{Q}_w=0 \quad \tilde{Q}_a=0 \quad \tilde{Q}_e=\tilde{Q}_{e0} \qquad \text{as } \eta\to 0 \tag{12}$$

$$P_g=P_0 \quad X_g^a=X_0 \quad S_g=S_0 \qquad \text{as } \eta\to\infty. \tag{13}$$

Further simplification is achieved by substituting $z=\ln\eta$, and replacing P_l with P_g+P_c

$$-\frac{1}{2}\frac{dM_m}{dz}+e^{-2z}\frac{d\tilde{Q}_m}{dz}=0 \quad \text{for } m=w,a \tag{14}$$

$$-\frac{1}{2}\frac{dM_e}{dz}+e^{-2z}\frac{d\tilde{Q}_e}{dz}=0 \tag{15}$$

$$\tilde{Q}_m=-(K_l X_l^m+K_g X_g^m)\frac{dP_g}{dz}-K_l X_l^m\frac{dP_c}{dz}-D_{va}\rho_g\frac{dX_g^m}{dz} \quad \text{for } m=w,a \tag{16}$$

$$\tilde{Q}_e=-\sum_{m=w,a}\left[(h_l^m K_l X_l^m+h_g^m K_g X_g^m)\frac{dP_g}{dz}+h_l^m K_l X_l^m\frac{dP_c}{dz}+h_g^m D_{va}\rho_g\frac{dX_g^m}{dz}\right]$$

$$-\kappa\frac{dT}{dz}. \tag{17}$$

The boundary conditions become

$$\tilde{Q}_w=0 \quad \tilde{Q}_a=0 \quad \tilde{Q}_e=\tilde{Q}_{e0} \qquad \text{as } z\to-\infty \tag{18}$$

$$P_g=P_0 \quad X_g^a=X_0 \quad S_g=S_0 \qquad \text{as } z\to\infty. \tag{19}$$

3. Solution of Equations

Equations (14-17) represent a set of six coupled first-order ordinary differential equations (ODE's). Solution of the system is straightforward in principle, by numerically integrating from $z = -\infty$ to $z = \infty$, but in practice two complications arise that require special numerical techniques. One difficulty is posed by the "mixed" boundary conditions, equations (18) and (19), which specify flux terms $\tilde{Q}_w$, $\tilde{Q}_a$, and $\tilde{Q}_e$ at $z = -\infty$, while the thermodynamic functions P_g, X_g^a, and S_g satisfy boundary conditions at $z = +\infty$. Thus no complete set of starting values is available for integration, and an iterative approach known as the shooting method [6] must be used (see below). Further difficulties arise from the non-linear dependence of the coefficients in equations (14-17) upon the thermodynamic parameters, especially in connection with multiphase flow effects (relative permeability, etc.) and phase change behavior.

We have achieved a computational solution for a simplified version of the problem stated by equations (14-17). The main simplification made is omission of the air component, which reduces the dimensionality of the problem from six coupled ODE's to a more easily tractable set of four ODE's. A further simplification is the restriction of admissible relative permeability functions to a mathematically well-behaved class of smooth functions. It is recognized that at the potential repository horizon at the Yucca Mountain site, significant flow effects will arise both from the presence of air [2] and from the extremely non-linear relative permeability relationships characteristic of a fractured-porous medium [7]. Our main objective in the present work has been to develop an accurate and computationally efficient implementation of the similarity solution technique under "mixed" boundary conditions, and to establish some reference cases for the behavior of strongly heat-driven flow systems with phase change. Work is underway to achieve a more realistic and detailed implementation of the specific conditions encountered at Yucca Mountain.

Shooting Method

The first step of the shooting method [6] is to choose trial values for the unspecified variables at the lower limit of integration $z_L = -\infty$. From the general description of the thermohydrologic behavior of the system given in Section 1, we know that at $z_L = -\infty$ (long times; close to the heat source) gas-phase conditions prevail, so the unspecified variables are P_g and T, which can be defined to be the components of a vector $\mathbf{V}$. The trial values at z_L are denoted P_L and T_L, or collectively $\mathbf{V}_L$. The numerical integration is then carried out from $z_L = -\infty$ to $z_U = \infty$. We use a fourth-order Runge-Kutta scheme, but other numerical integration algorithms could be used. The value of $\mathbf{V}$ at the upper limit of integration z_U is denoted $\mathbf{V}_U$; it can be viewed as a function of $\mathbf{V}_L$. When air is not included in the analysis, liquid-phase conditions prevail at $z_U = \infty$ (initial time; far from the heat source) so the primary variables are P_g and T, and $\mathbf{V}_U$ has components P_U and T_U. Boundary conditions are specified at z_U for each component of $\mathbf{V}$, so we can define a discrepancy vector $\mathbf{F}$, as the difference between $\mathbf{V}_U$ and the specified boundary conditions at z_U. The goal is to find an improved value of $\mathbf{V}_L$, denoted $\mathbf{V}_L^*$, that reduces the absolute value of $\mathbf{F}$ below an acceptable limit. We accomplish this via Newton-Raphson iteration; that is, we solve the following equation for $\mathbf{V}_L^*$

$$\mathbf{R}(\mathbf{V}_L^* - \mathbf{V}_L) = -\mathbf{F} \tag{20}$$

where $\mathbf{R}$ is the Jacobian matrix, with components R_{ij} $(i, j = 1,2)$ given by

$$R_{ij} = \frac{\partial F_i}{\partial V_{Lj}}. \tag{21}$$

The components of the matrix $\mathbf{R}$ are obtained by numerical differentiation. This requires two additional numerical integrations each using a modified value for one component of $\mathbf{V}_L$, denoted $V_{Lj} + \delta V_{Lj}$. The partial derivatives of equation (21) are then approximated by

$$\frac{\partial F_i}{\partial V_{Lj}} \approx \frac{F_i(V_{L1}, \cdots, V_{Lj} + \delta V_{Lj}, \cdots) - F_i(V_{L1}, \cdots, V_{Lj}, \cdots)}{\delta V_{Lj}}. \tag{22}$$

In general, because the equations are non-linear, a numerical integration initialized with $\mathbf{V}_L^*$ will not yield a zero value for $\mathbf{F}$, so the procedure must be repeated. Iteration continues until $|F_i| < \gamma |V_{Ui}|$, and $|V_{Li}{}^* - V_{Li}| < \gamma |V_{Li}|$ for $i = 1,2$, where γ represents the desired accuracy for $\mathbf{V}_L$ and $\mathbf{V}_U$.

In a numerical procedure, using truly infinite integration limits is impossible; infinity must be approximated by suitably large finite values. (As will be seen later, due to the nature of the present problem the solution is insensitive to the values of the integration limits if they are beyond a certain range.)

To use the shooting method, we need to express the governing equations in terms of derivatives of the primary variables with respect to the similarity variable. This is done through use of the chain rule for partial derivatives. Recall that different sets of primary variables are applicable for single- and two-phase conditions.

When air is not included in the analysis only the $m = w$ terms of equations (14-17) are needed, since X^a and $\tilde{Q}_a$ are equal to zero for all z. In the following, the superscript w is omitted when no ambiguity results.

ODE's for Single-phase Regions

The distinction between P_g and P_l is not meaningful when only one phase exists, so the pressure is referred to simply as P in single-phase regions, and the chain rule takes the form

$$\frac{d}{dz} = \frac{dP}{dz}\frac{\partial}{\partial P} + \frac{dT}{dz}\frac{\partial}{\partial T} \tag{23}$$

and equations (14-17) become

$$-\frac{1}{2}\left(\frac{\partial M_w}{\partial P}\frac{dP}{dz} + \frac{\partial M_w}{\partial T}\frac{dT}{dz}\right) + e^{-2z}\frac{d\tilde{Q}_w}{dz} = 0 \tag{24}$$

$$-\frac{1}{2}\left(\frac{\partial M_e}{\partial P}\frac{dP}{dz} + \frac{\partial M_e}{\partial T}\frac{dT}{dz}\right) + e^{-2z}\frac{d\tilde{Q}_e}{dz} = 0 \tag{25}$$

$$\tilde{Q}_w = - K_j \frac{dP}{dz} \tag{26}$$

$$\tilde{Q}_e = - h_j K_j \frac{dP}{dz} - \kappa \frac{dT}{dz}. \tag{27}$$

The subscript j is g for the gas phase and l for the liquid phase, labeled zones 1 and 4, respectively, in Figure 1. Capillary pressure P_c is constant in single-phase regions, so $dP_c/dz = 0$. The accumulation terms simplify to

$$M_w = \phi \rho_j \tag{28}$$

$$M_e = (1-\phi)\rho_r c_r T + \phi \rho_j u_j . \tag{29}$$

We would like to rearrange equations (24-27) to isolate the z-derivative terms on the left-hand-side. Equation (26) can be trivially solved for dP/dz, which can then be substituted into (27) to yield an expression for dT/dz. Equations (24) and (25) can be easily solved for $d\tilde{Q}_w/dz$ and $d\tilde{Q}_e/dz$, respectively, in terms of dP/dz and dT/dz. Altogether we obtain the following set of equations to integrate for zones 1 and 4

$$\frac{dP}{dz} = -\frac{\tilde{Q}_w}{K_j} \tag{30}$$

$$\frac{dT}{dz} = -\frac{\tilde{Q}_e - h_j \tilde{Q}_w}{\kappa} \tag{31}$$

$$\frac{d\tilde{Q}_w}{dz} = \frac{e^{2z}}{2}\left(\frac{\partial M_w}{\partial P}\frac{dP}{dz} + \frac{\partial M_w}{\partial T}\frac{dT}{dz} \right) \tag{32}$$

$$\frac{d\tilde{Q}_e}{dz} = \frac{e^{2z}}{2}\left(\frac{\partial M_e}{\partial P}\frac{dP}{dz} + \frac{\partial M_e}{\partial T}\frac{dT}{dz} \right). \tag{33}$$

ODE's for Two-phase Regions

For two-phase regions the chain rule takes the form

$$\frac{d}{dz} = \frac{dP_g}{dz}\frac{\partial}{\partial P_g} + \frac{dS_g}{dz}\frac{\partial}{\partial S_g} \tag{34}$$

and equations (14-17) become

$$-\frac{1}{2}\left(\frac{\partial M_w}{\partial P_g}\frac{dP_g}{dz}+\frac{\partial M_w}{\partial S_g}\frac{dS_g}{dz}\right)+e^{-2z}\frac{d\tilde{Q}_w}{dz}=0 \tag{35}$$

$$-\frac{1}{2}\left(\frac{\partial M_e}{\partial P_g}\frac{dP_g}{dz}+\frac{\partial M_e}{\partial S_g}\frac{dS_g}{dz}\right)+e^{-2z}\frac{d\tilde{Q}_e}{dz}=0 \tag{36}$$

$$\tilde{Q}_w=-\left[K_l\left(1+\frac{\partial P_c}{\partial P_g}\right)+K_g\right]\frac{dP_g}{dz}-\left[K_l\frac{\partial P_c}{\partial S_g}\right]\frac{dS_g}{dz} \tag{37}$$

$$\tilde{Q}_e=-\left[h_l K_l\left(1+\frac{\partial P_c}{\partial P_g}\right)+h_g K_g+\kappa\frac{dT}{dP_g}\right]\frac{dP_g}{dz}-\left[h_l K_l\frac{\partial P_c}{\partial S_g}\right]\frac{dS_g}{dz}. \tag{38}$$

Here we have neglected vapor pressure lowering effects, so that in equation (38) there is no $\partial T/\partial S_g$ term, and the $\partial T/\partial P_g$ term is replaced by dT/dP_g. This reflects the simple dependence of temperature on pressure through the saturation curve. Note from equations (4) and (5) that the accumulation terms M_w and M_e contain terms ρ_l, ρ_g, u_l, u_g, and ϕ that depend on pressure both explicitly, and implicitly through temperature, since $T=T_{\mathrm{sat}}(P_g)$.

As in the single-phase region, we would like to rearrange (35-38) to explicitly obtain dP_g/dz and dS_g/dz from equations (37) and (38), so that the remaining unknowns $d\tilde{Q}_w/dz$ and $d\tilde{Q}_e/dz$ can be found by simple substitution into (35) and (36). To accomplish this it is necessary to divide by K_l, which is proportional to the liquid relative permeability, k_{rl}. By definition, $k_{rl}>0$ when $S_l>S_{lr}$, where S_{lr} is the residual liquid saturation. In the present work, to avoid the complications arising from $K_l=0$ for $S_l\leq S_{lr}$, we only consider cases where $S_{lr}=0$, so $k_{rl}>0$ throughout the two-phase zone, and there is never a problem dividing by K_l. A two-phase region with a mobile liquid phase is shown as zone 3 in Figure 1. In future work we plan to address the situation where $S_{lr}>0$ and a two-phase zone with an immobile liquid phase develops (zone 2 in Figure 1).

With the condition $K_l > 0$, equations (37) and (38) can be solved for dP_g/dz and dS_g/dz. Equations (35) and (36) can be solved for $d\tilde{Q}_w/dz$ and $d\tilde{Q}_e/dz$, respectively, in terms of dP_g/dz and dS_g/dz. Altogether we obtain the following set of equations to integrate for zone 3

$$\frac{dP_g}{dz} = -\frac{\tilde{Q}_e - h_l \tilde{Q}_w}{(h_g - h_l)K_g + \kappa \frac{dT}{dP_g}} \tag{39}$$

$$\frac{dS_g}{dz} = \frac{\tilde{Q}_e \left[K_l \left(1+\frac{\partial P_c}{\partial P_g}\right)+K_g\right] - \tilde{Q}_w \left[h_l K_l \left(1+\frac{\partial P_c}{\partial P_g}\right)+h_g K_g + \kappa \frac{dT}{dP_g}\right]}{\left[(h_g - h_l)K_g + \kappa \frac{dT}{dP_g}\right] K_l \frac{\partial P_c}{\partial S_g}} \tag{40}$$

$$\frac{d\tilde{Q}_w}{dz} = \frac{e^{2z}}{2}\left(\frac{\partial M_w}{\partial P_g}\frac{dP_g}{dz} + \frac{\partial M_w}{\partial S_g}\frac{dS_g}{dz}\right) \tag{41}$$

$$\frac{d\tilde{Q}_e}{dz} = \frac{e^{2z}}{2}\left(\frac{\partial M_e}{\partial P_g}\frac{dP_g}{dz} + \frac{\partial M_e}{\partial S_g}\frac{dS_g}{dz}\right). \tag{42}$$

Transitions Between Zones

In order to make the transition in primary variables required at phase changes, at each step in the numerical integration the current phase conditions are checked. For the gas-phase (zone 1), as equations (30-33) are being integrated, the temperature T is compared to the saturation temperature for the pressure, $T_{\text{sat}}(P)$. If $T > T_{\text{sat}}+\epsilon$, where $\epsilon \approx 10^{-8}$, the gas-phase/two-phase transition has not been reached yet. The integration step is accepted, and the integration proceeds, still in zone 1. If $T < T_{\text{sat}}-\epsilon$, the integration has gone beyond the phase change point. The step is then rejected and attempted again using a smaller step size. If $T_{\text{sat}}-\epsilon < T < T_{\text{sat}}+\epsilon$, the phase change point has been reached, and the transition to two-phase conditions (zone 3) is made, with gas-phase saturation S_g replacing T as the primary variable, and equations (39-42) replacing (30-33) in the integration. At the zone 1/zone 3 transition, S_g is initialized as $1-S_l^{\min}$,

where $S_l^{\min}$ is the minimum liquid saturation for which liquid relative permeability $k_{rl} > \epsilon$. The value of $S_l^{\min}$ depends on the form of the relative permeability function.

At each step in zone 3, as equations (39-42) are being integrated, T is set to $T_{\text{sat}}(P_g)$ and S_g is compared to zero. If $S_g > \epsilon$, the two-phase/liquid transition has not been reached yet; the step is accepted, and the integration proceeds, still in zone 3. If $S_g < -\epsilon$, the phase change point has been passed. The step is then rejected and repeated using a smaller step size. If $-\epsilon < S_g < \epsilon$, the phase change point has been reached, and the transition to zone 4 is made, with T becoming the primary variable, and equations (30-33) replacing (39-42) in the integration.

The parameter ϵ is chosen to be very small compared to the numbers it is added to or multiplied by, but large enough to be treated accurately by a finite-precision computer. We take $\epsilon = 10^{-n}$, where n is half the number of significant figures the computer uses to express real numbers. The present work was done on a Cray X-MP at the National Magnetic Fusion Energy Computer Center, Lawrence Livermore National Laboratory, which expresses real numbers with approximately 16 significant figures, so $\epsilon = 10^{-8}$.

Step-size Control

At each step in the numerical integration, the results are compared with results obtained by splitting the step into two half-steps. If the results agree within a specified criterion, the step is accepted and step size is increased for the next step; if they do not, the step is rejected and repeated using a smaller step size.

4. Computational Procedure

As an example of the application of the similarity solution, we consider a heat source of strength Q_{e0}=200 W/m emplaced in a porous medium with material properties and characteristic curves given in Table 1, with initial conditions P_0=0.1013 MPa and T_0=26 °C. For the most part the properties and functions described in Table 1 are representative of a laboratory sand pack used to study steady-state heat-pipe behavior [8]. The intrinsic permeability k has been decreased by a factor of 10, and the rock compressibility $\beta_r = (1/\phi)\partial\phi/\partial P$ increased by a factor of 10 to create a more computationally efficient example. Neither change is necessary for the method to work in general; the effects of the changes are described later in this section.

The first step when applying the similarity solution is to choose z_L and z_U, the limits of integration, and trial values for T and P at z_L, which are denoted $T(z_L)=T_L$ and $P(z_L)=P_L$. Some clues are provided by examining the much simpler problem of a heat source emplaced in a medium in which all heat transfer is conductive. For constant thermal conductivity κ_c and heat capacity C_c this problem has an analytical solution given in terms of the exponential integral [14]

$$Q_e = \frac{Q_{e0}}{2\pi}\exp\left(\frac{-C_c\,\eta^2}{4\kappa_c}\right) \tag{43}$$

$$T = T_0 + \frac{Q_{e0}}{2\pi\kappa_c}\int_{\eta}^{\infty}\frac{1}{\eta}\exp\left(\frac{-C_c\,\eta^2}{4\kappa_c}\right)d\eta = T_0 - \frac{Q_{e0}}{4\pi\kappa_c}\mathrm{EI}\left(\frac{-C_c\,\eta^2}{4\kappa_c}\right). \tag{44}$$

Figure 2 shows the temperature and heat-flow profiles for thermal properties corresponding to liquid water (κ_c =1.13 W/m °C, C_c =2.9 MJ/m^3 °C) and water vapor (κ_c =0.582 W/m °C, C_c =1.3 MJ/m^3 °C) saturating a medium with thermal properties given in Table 1. Appropriate limits of integration for this problem would be z_L <−11 and z_U >−5, beyond the region of changing heat flow. Anticipating variations in fluid flow as well as heat flow, we arbitrarily extend the limits in both direction to obtain z_L =−15 and z_U =−3 as tentative limits for the similarity-solution integration. For a vanishingly

short heat pipe, that is, a direct transition from gas to liquid phase, T_L would fall between the $T(z_L)$ values for the liquid and gas curves shown in Figure 2, 252 °C and 468 °C. Thus, we take T_L =(252+468)/2=360 °C as an initial guess for the temperature boundary condition. If the heat-pipe region turns out to be substantial, this value of T_L will be too high. The conduction solution does not provide any information on pressure so we take $P_L = P_0$=0.1013 MPa.

The numerical integration from z_L =−15 to z_U =−3 results in T_U =45.6 °C and P_U =0.0509 MPa (Table 2). For this "first shot", T_U and P_U are not very close to T_0 or P_0, which is not surprising in view of the simplistic initial guesses used. The Newton-Raphson iteration requires that the integration be repeated twice for each shot, using a modified value of P_L, $P_L + \delta P_L$, in one case, and a modified value of T_L, $T_L + \delta T_L$, in the other. The values chosen for δP_L and δT_L must be small enough to yield an accurate approximation for the partial derivatives given in equation (22), but large compared to the errors generated in the numerical integration. By comparing $P_U - P_0$ and $T_U - T_0$ for the three integrations, improved values of P_L and T_L are obtained for the second shot. After three shots the solution converges, as shown in Table 2. Figure 3 shows the temperature and pressure profiles for each shot. (In all figures, pressure shown in the two-phase region is P_g.) Each integration takes about 420 steps; the whole procedure uses 20 seconds of CPU time on a Cray X-MP computer.

Sometimes an initial guess may be too poor to allow the numerical integration to be completed. For example, if T_L is too small, temperatures drop below 0 °C and the equations of state for liquid water and vapor are not applicable. Without values of T_U and P_U, the Newton-Raphson iteration cannot be done. Other times the integration can be completed, but the T_U and P_U values are so far from T_0 and P_0 that the Newton-Raphson iteration diverges. In practice, the usual procedure is to perform a numerical integration with an initial guess for T_L and P_L, plot the resulting T and P profiles, and choose improved values of T_L and P_L based on general features of the profiles. After

one or two repetitions of this procedure, the profiles should be close enough to the true solution to allow efficient use of Newton-Raphson iteration.

Figure 4a shows the pressure, temperature, and saturation profiles for the converged solution, while the solid lines in Figure 4b show the liquid, gas, water (liquid plus gas), and heat flow-rate profiles. The lower limit of integration, z_L, is beyond the region where fluid or heat flow vary, but at $z_U = -3$, Q_l is still changing, so the integration should be continued. Both T and P are nearly constant around $z = -3$, so extending the integration will not require additional Newton-Raphson iterations. The dashed line shows Q_l, Q_g, and Q_e values obtained by continuing the integration from $z_L = -3$ to $z_U = -1.4$. This part of the integration requires 6780 steps, significantly more than the 420 required to integrate between $z_L = -15$ and $z_U = -3$. The form of equations (32) and (33) dictates that as z increases, step size decreases. This decrease becomes significant for $z > -5$, and overwhelming for $z > -1$.

Note from the definition of the similarity variable that Figure 4 represents both a spatial distribution at a given time, with distance from the heat source increasing from left to right, and a time sequence at a given point in space, with time increasing from right to left. The signature of the heat pipe is the large liquid-vapor counterflow shown in Figure 4b, with net water flow nearly zero, and the corresponding nearly isothermal zone shown in Figure 4a. The larger temperature gradient and constant pressure within the vapor zone ($z < -11.8$) indicate that conduction is the dominant heat-transfer mechanism there. In the liquid zone ($z > -9.6$) there are two domains. Just beyond the two-phase zone there is a region with a linear temperature gradient and small mass flow, indicating a conductive regime. Beyond the leading edge of the heat flow front ($z \approx -7$), there is a liquid flow away from the heat source, with attendant small sensible heat transport, that arises because the water vapor forming at the heat pipe is much less dense than the liquid water it replaces.

5. Comparison with Numerical Simulations

The numerical model TOUGH [15] has been used to verify the similarity solution. TOUGH (**T**ransport **O**f **U**nsaturated **G**roundwater and **H**eat) calculates the two-phase flow of air and water in gaseous and liquid phases together with heat flow using the governing equations shown in Section 2. Material properties vary with pressure, temperature, and saturation as described in Appendix A. TOUGH uses an integral finite difference method that is applicable for one-, two-, or three-dimensional flow problems in porous or fractured porous media. The governing mass- and energy-balance equations are strongly nonlinear and are solved simultaneously, using Newton-Raphson iteration.

A one-dimensional radial calculational mesh with 90 elements is used to calculate pressure, temperature, and saturation in a porous medium surrounding a heat source of strength Q_{e0}=200 W/m. Material properties and mesh dimensions are given in Table 3. Initial conditions everywhere are $P = 0.1013$ MPa, $T = 26\,^{\circ}$C, and $S_l = 1$. The innermost element of the mesh includes the heat source; at the outermost element P and T are held constant. This approximate implementation of the similarity-solution boundary conditions for $z = -\infty$ and $z = \infty$ is unavoidable with a numerical model, which is necessarily of finite extent.

A simulation for 10,000 years takes 475 time steps and requires 8.6 minutes of CPU time on a Cray X-MP. Figure 5, which shows temperature, pressure, and saturation (5a) and heat, mass, liquid, and gas flows (5b) versus radial distance for a series of times, illustrates the development of the heat pipe and its migration away from the heat source. Figure 6 shows the same variables plotted as a function of $z = \ln(r/\sqrt{t})$, with profiles for 21 different times displayed. The close agreement between the profiles for different times verifies the use of the similarity concept for this problem. The small spread between the profiles can be understood from the observation by Schroeder et al. [16], that for a numerical solution calculated on a finite-difference grid, there is only an approximate invariance with respect to the similarity variable, due to the finite grid

spacing. Data from the innermost and outermost mesh elements are not included in Figure 6 because grid effects are most pronounced where boundary conditions are implemented. The greater spread between the profiles at the inner limit of the heat pipe results from early-time profiles, when the heat source is close to the heat pipe. Later-time profiles, when the heat pipe has moved further from the heat source, are more accurate. At still later times, the liquid flow away from the heat source reaches the constant-pressure boundary at the outer limit of the mesh, so the mesh no longer represents an infinite medium properly, causing the liquid flow profiles to diverge. Figure 7 compares an intermediate-time profile, for which mesh effects are minimal, and the similarity solution. The match is excellent.

6. Illustrative Examples

In this section we examine significant features of the response of a porous medium to emplacement of a strong heat source in one-dimensional radial geometry. In particular, the dependence of system behavior upon major thermal and hydrologic parameters is illustrated by way of calculated examples.

Relative Permeability Functions

Five different relative permeability functions are described in Table 4, and plotted in Figure 8a as a function of liquid saturation S_l. The linear, cubic [11, 12], and Corey [17] functions are commonly encountered in the petroleum literature, the Verma et al. [18] function was developed from laboratory experiments on liquid-vapor water flow, and the van Genuchten [19] liquid relative permeability function comes from the soil sciences. As is traditional in the soil-science approach to fluid flow, no gas-phase relative permeability function is presented in the van Genuchten work [19], so we take $k_{rg} = 1 - k_{rl}$. For the parameter λ we use 0.45 [20]. Figure 8b shows the temperature, pressure, and saturation profiles calculated with the different relative permeability functions, using the other values from Table 1. A large variation in heat-pipe length is seen. The cubic and Corey curves (Figure 8a) are quite similar, and yield similar profiles (Figure 8b), with relatively short heat pipes. The linear and Verma curves (Figure 8a) are similar for k_{rg}, but quite different for k_{rl}. The corresponding saturation profiles (Figure 8b) are similar for large values of S_l, but very different for $S_l < 0.25$, resulting in very different length heat pipes. The van Genuchten k_{rg} curve is quite different from all the others, and the resulting saturation profile is also distinct, but the heat-pipe length is similar to that for the linear curves. Note that the linear and van Genuchten curves share the property that $k_{rl} + k_{rg} = 1$ (for the other cases $k_{rl} + k_{rg} < 1$) and that the heat-pipe length is significantly greater for these cases.

The effect of the relative permeability function can be predicted qualitatively by examining equation (40) for dS_g / dz. To facilitate comparison with the figures, which

show S_l rather than S_g, we replace dS_g/dz with $-dS_l/dz$

$$\frac{dS_l}{dz} = -\frac{\tilde{Q}_e\left[K_l\left(1+\frac{\partial P_c}{\partial P_g}\right)+K_g\right]-\tilde{Q}_w\left[h_l K_l\left(1+\frac{\partial P_c}{\partial P_g}\right)+h_g K_g+\kappa\frac{dT}{dP_g}\right]}{\left[(h_g-h_l)K_g+\kappa\frac{dT}{dP_g}\right]K_l\frac{\partial P_c}{\partial S_g}}. \tag{45}$$

When heat-pipe effects are significant, as in the examples shown in Figures 4a, 4b, and 8b, equation (45) can be simplified. Figure 4b shows that in the two-phase region net water flow Q_w is zero and heat flow Q_e is constant. Furthermore, $\partial P_c/\partial P_g$ is generally small, and $\kappa dT/dP_g$ is small compared to $(h_g-h_l)K_g$ if conduction is small compared to convection, that is, if the heat-pipe region is nearly isothermal. Thus an approximate version of equation (45) may be written

$$\frac{dS_l}{dz} \approx -\frac{\tilde{Q}_e}{(h_g-h_l)\frac{\partial P_c}{\partial S_g}}\left[\frac{K_l+K_g}{K_g K_l}\right] = \frac{\tilde{Q}_e}{(h_g-h_l)\frac{\partial P_c}{\partial S_g}}\left[\frac{1}{K_g}+\frac{1}{K_l}\right] \tag{46}$$

where $K_g = kk_{rg}\rho_g/\mu_g$ and $K_l = kk_{rl}\rho_l/\mu_l$. Under the nearly constant-temperature constant-pressure conditions of the heat-pipe region, ρ_g, ρ_l, μ_g, and μ_l are approximately constant, and can be combined into a parameter β, defined as the ratio of the kinematic viscosities of the liquid and gas.

$$\beta = \frac{\mu_l/\rho_l}{\mu_g/\rho_g}. \tag{47}$$

For $P_g \approx 0.1$ MPa and $T \approx 100\,^\circ$C, $\beta \approx 0.01$. Equation (46) may then be written

$$\frac{dS_l}{dz} \approx -\frac{\tilde{Q}_e}{(h_g-h_l)\frac{\partial P_c}{\partial S_g}\frac{k\rho_g}{\mu_g}}\left[\frac{1}{k_{rg}}+\frac{\beta}{k_{rl}}\right]. \tag{48}$$

Thus dS_l/dz is controlled by the smaller of k_{rg} and k_{rl}/β. For large values of S_l, k_{rg} is the controlling factor. Figure 8a shows that the value of k_{rg} for the van Genuchten function is far larger than the rest, while the cubic and Corey functions are similar and

very small, and the linear and Verma functions are similar and of intermediate magnitude. This variation is reflected in the upper portion of the saturation profiles in Figure 8b, where the van Genuchten S_l profile has the smallest slope, the cubic and Corey profiles are steepest, and the linear and Verma profiles are in between. For small values of S_l, k_{rl} is the controlling factor. Figure 8a shows that the values of k_{rl} for the linear and Verma functions are very different, leading to the diverging saturation profiles seen in Figure 8b. The k_{rl} curves for the cubic and Corey functions are similar, so the saturation profiles remain close together. The Verma and cubic functions use the same k_{rl} curve, as evidenced by the parallel saturation profiles for small values of S_l. All the k_{rl} curves except the linear one become vanishingly small as S_l approaches zero, leading to the sharp downturn in saturation profile characteristic of all cases except the linear one.

Intrinsic Permeability

Figure 9 shows the temperature, pressure, and saturation (Figure 9a), and the liquid, gas, water, and heat flow (Figure 9b) profiles calculated for three rather large values of intrinsic permeability, $k = 10^{-12}$, 10^{-13}, and 10^{-14} m^2, using the Verma et al. [18] relative permeability functions (Table 4), and the other values from Table 1. The most striking feature of Figure 9a is the large decrease in heat-pipe length with decreasing permeability. Additionally, both heat-pipe temperature and temperature gradient increase with decreasing permeability, because a larger pressure gradient is needed to drive fluid flow, and temperature depends on pressure through $T_{\rm sat}(P_g)$. Conduction increases in the heat-pipe region as it becomes less isothermal. Figure 10 shows the same profiles for lower values of intrinsic permeability, $k = 10^{-15}$ and 10^{-17} m^2, again using the Verma relative permeability functions and the other values from Table 1. In the heat-pipe region, conduction becomes increasingly important relative to convection as permeability decreases, until for $k = 10^{-17}$m^2 there is virtually no heat-pipe effect seen in Figure 10a. Because the saturation profile is quite sharp, the temperature profile for this case is

very similar to the conduction-only profiles shown in Figure 2; the liquid T profile is followed while $S_l > 0$, and a transition is made to the gas T profile at $S_l = 0$. In Figures 9b and 10b, the Q_g and Q_l profiles illustrate the decrease in heat-pipe counterflow for decreasing permeability. When permeability is large (Figure 9b, $k = 10^{-12}$ and 10^{-13} m^2), the counterflow is large enough to transfer all heat convectively and an extended region of constant Q_g and Q_l develops, corresponding to the isothermal zone seen in Figure 9a. For $k = 10^{-14}$ m^2, this region disappears. For smaller values of permeability (Figure 10b), there is no region of constant Q_g and Q_l, and the peak flow decreases in magnitude and shifts to more negative values of z. Despite the very different fluid flow patterns seen in Figures 9b and 10b, the heat flow profile remains unchanged.

Heat Source Strength

Figure 11 shows temperature and pressure (Figure 11a), liquid, gas, and water flow (Figure 11b), and heat flow (Figure 11c) profiles calculated for heat source strength values of $Q_{e0} = 100$, 200, 500, and 1000 W/m using the Verma relative permeability functions and the other values from Table 1. Figure 11a shows that larger values of Q_{e0} yield a shorter heat pipe, and steeper conduction gradients, which shift the heat pipe to larger values of z. The overall pressure increase does not change very much with variations in Q_{e0}, so the heat-pipe temperature remains nearly constant.

Figures 11b and 11c show that the magnitude of the liquid-vapor counterflow is directly proportional to Q_e, demonstrating that heat transfer is convection-dominated. In the liquid region beyond the heat pipe, liquid flow away from the heat source increases in magnitude with increasing Q_{e0}. Recall from the definition of z that a shift in heat-pipe location to larger values of z represents a heat pipe moving away from the heat source more rapidly, indicating more vapor formation, thus requiring larger flow of liquid away from the heat source.

For low values of Q_{e0} (100 and 200 W/m) the heat-pipe region (with liquid flow toward the heat source) and outer liquid-flow region (with liquid flow away from the heat source) are well separated, but as Q_{e0} increases and the conduction gradients become steeper, these two zones begin to overlap, resulting in a net decrease in the magnitude of liquid flow. Since vapor flow does not similarly decrease, there results a non-zero water (liquid plus vapor) flow in the heat-pipe region, and a corresponding increase in heat flow, as shown in Figure 11c. Further, for higher values of Q_{e0}, the heat pipe occurs at such large values of z, that the Q_e profile has already begun to decrease when the heat pipe begins, leading to an oscillation in Q_e.

Capillary Pressure Function

As is the case with relative permeability functions, a variety of capillary pressure functions have been used to describe fluid flow through porous media. Unlike relative permeabilities, which always vary between zero and one, the magnitude of the capillary pressure depends on other physical properties of the system, making it difficult to isolate the influence of capillary pressure function. Equation (48) shows that saturation-profile slope is inversely proportional to $\partial P_c / \partial S_g$. However, we have seen that this slope is controlled by the liquid relative permeability function when S_l is small. Hence capillary pressure functions that vary over the entire range of S_l, rather than primarily near S_{lr}, tend to produce longer heat pipes.

Rock Compressibility

The value of rock compressibility, $\beta_r = 10^{-7}$ Pa^{-1}, used in the above examples is an order of magnitude greater than typical values found in nature. A calculation for the problem described in Table 1, using a more realistic value of $\beta_r = 10^{-8}$ Pa^{-1} yields identical results to those shown in Figure 4, except that the outer liquid flow extends to larger values of z. As noted previously, small integration steps are necessary for large values of z, so extending the limits of integration to large z requires increased computational effort. As long as the rock compressibility used is small relative to gas-phase and two-

phase water compressibilities it will only affect the solution in the liquid zone.

Initial Conditions

Initial temperature, T_0, and pressure, P_0, greatly influence the fluid and heat flows that occur in response to a heat source. For a heat pipe to develop the fluid must be volatile, that is, near its saturation temperature, which is determined by P_0. For partially saturated media, T_0 increases with depth while P_0 and therefore saturation temperature remain essentially constant. Thus the transition from zone 4 to zone 3 (see Figure 1), which happens when $T \approx T_{sat}$, occurs at larger values of η (earlier times) for deeper heat sources. For fully saturated media, both T_0 and P_0 increase as depth increases, with $T_{sat}(P_0)$ growing faster than T_0. Thus the zone 4/zone 3 transition occurs at smaller values of η (later times) for deeper heat sources. Equation (44) for the conduction-only temperature distribution may be used to determine η_{sat}, the largest value of η for which $T = T_{sat}$. For a given radial distance, η_{sat} determines the earliest time after waste emplacement when saturation temperature is reached, denoted t_{sat}. Table 5 shows t_{sat} for various heat-source depths, calculated using equation (44), and a value of $r = 0.25$ m. It is apparent that P_0 plays the dominant role in controlling t_{sat}. Allowing for the heat-source strength decline with time characteristic of nuclear waste repositories, it is unlikely that saturation temperature will ever be reached for the fully saturated cases in Table 5.

Table 6 shows t_{sat} for some proposed repository conditions. As expected, t_{sat} is smallest for the partially saturated Yucca Mountain site. The value of t_{sat} is also quite small for the Stripa site, despite the large value of P_0, due to the high heat flow rate, Q_{e0}=1385 W/m. Similarly, the large value of t_{sat} for the Mol-Dessel site is largely due to the low heat flow rate Q_{e0}=300 W/m.

The P_0 values in Table 6 assume that the initial repository pressure is equal to the ambient pressure. For repositories in fully saturated media, this is not a good

assumption if the repository is ventilated with atmospheric air, or if backfill pressure is less than ambient pressure. In this case, non-uniform initial conditions preclude use of the similarity transformation and the results presented in this paper are not applicable. Although two-phase conditions may evolve, heat-pipe development is not expected under these circumstances, because a heat pipe requires a driving force for gas-phase flow away from the heat source, which is absent if the pressure at the heat source is less than the ambient pressure.

7. Summary and Conclusions

The mass and energy transport equations for one-dimensional radial flow in a homogeneous porous medium depend on time t and distance r only through the similarity variable $\eta = r/\sqrt{t}$. If initial and boundary conditions can be written as functions of η, then the entire flow problem admits a solution in terms of the similarity variable. A practically important case where this is possible is for a constant-rate line source at $r = 0$, and uniform initial conditions.

We have applied the similarity variable concept to solve an idealized version of the problem of fluid and heat flow near high-level nuclear waste packages emplaced in geologic media. The cylindrical waste package is approximated by a linear heat source at $r = 0$. By means of the similarity transformation, the partial differential equations for fluid and heat flow are converted to a set of ordinary differential equations in η. These can be efficiently solved with the iterative "shooting method". The accuracy and efficiency of the similarity solution approach has been demonstrated by comparison with numerical finite-difference simulations. Illustrative examples have been presented to show the dependence of fluid and heat flow patterns and heat pipe conditions on relative and absolute permeability, and other parameters of interest.

The most important application of the approach developed in this paper is for the evaluation of thermohydrologic conditions that will develop near high-level nuclear waste packages emplaced in the partially saturated fractured tuffs at Yucca Mountain. A realistic appraisal will require solving the full equation system, including air, and making provisions for dealing with the extremely non-linear relative permeability relationships characteristic of a fractured-porous medium [7]. This appears quite feasible and is currently under development. A peculiar issue in nuclear waste disposal arises from the decline of heat output with time. However, the constant-rate solution obtainable from the similarity method will give an acceptable approximation for the early-time period (tens of years) when thermal effects in the host rock are strongest. Long-time

predictions from a constant-rate heat source are also useful because they provide conservative limits for thermohydrologic effects. The similarity solution can also serve as a benchmark for testing the accuracy of complex numerical simulators for multiphase fluid and heat flow.

Acknowledgements

The careful review of this work by Y. W. Tsang and R. W. Zimmerman is gratefully appreciated. This work was supported, in part, by the NNWSI Performance Assessment Division, Sandia National Laboratories, and the Director, Office of Energy Research, Office of Basic Energy Sciences, Division of Engineering and Geosciences, of the U.S. Department of Energy under Contract No. DE-AC03-76SF00098.

References

1. K. Pruess, Y. W. Tsang, and J. S. Y. Wang, Modeling of strongly heat driven flow in partially saturated fractured porous media. In *Memoirs, International Association of Hydrogeologists*, Vol. XVII, pp. 486-497 (1985).

2. C. Doughty and K. Pruess, A semianalytical solution for heat pipe effects near high-level nuclear waste packages buried in partially saturated geological media. *Int. J. Heat Mass Transfer* **31**(1), 79-90 (1988).

3. M. J. O'Sullivan, A similarity method for geothermal well test analysis. *Water Resour. Res.* **17**(2), 390-398 (1981).

4. M. A. Grant, Quasi-analytic solutions for two-phase flow near a discharging well. *Rep. 86*, Appl. Math. Div., Dep. of Sci. and Ind. Res., Wellington, N.Z. (1979).

5. Y. W. Tsang and C. F. Tsang, An analytic study of geothermal reservoir pressure response to cold water reinjection. Presented at the Fourth Annual Workshop on Geothermal Reservoir Engineering, Stanford University, Dec. 13-15 (1978).

6. W. H. Press, B. P. Flannery, S. A. Teukolsky, and W. T. Vetterling, *Numerical Recipes: The art of scientific computing.* Cambridge University Press, New Rochelle, New York, Ch. 16 (1986).

7. K. Pruess, J. S. Y. Wang, and Y. W. Tsang, On thermohydrological conditions near high-level nuclear wastes emplaced in partially saturated fractured tuff. Part 2: effective continuum approximation. Submitted to Water Resour. Res. (1988).

8. K. S. Udell and J. S. Fitch, Heat and mass transfer in capillary porous media considering evaporation, condensation, and non-condensible gas effects. In *Heat Transfer in Porous Media and Particulate Flows*, HTD Vol. 46, *Proceedings of the 23rd ASME/AIChE National Heat Transfer Conf.*, Denver, 4-7 August (1985).

9. W.H. Somerton, J.A. Keese and S.L. Chu, Thermal behavior of unconsolidated oil sands, *Pap. SPE-4506*, presented at 48th Annual Fall Meeting of the Society of

Petroleum Engineers, Las Vegas (1973).

10. W.H. Somerton, A.H. El-Shaarani and S.M. Mobarak, High temperature behavior of rocks associated with geothermal type reservoirs, *Pap. SPE-4897*, presented at 44th Annual California Regional Meeting of the Society of Petroleum Engineers, San Francisco (1974).

11. I. Fatt and W.A. Klikoff, Effect of fractional wettability on multiphase flow through porous media, AIME Technical Note #2043, *AIME Trans.* **216**, 246 (1959).

12. M.R.J. Wyllie, Relative permeability, in *Petroleum Production Handbook* (T. C. Frick, Ed.), Vol. 2, Ch. 25, McGraw-Hill, New York (1962).

13. M.C. Leverett, Capillary behavior in porous solids, *AIME Trans.* **142**, 152-169 (1941).

14. H. S. Carslaw and J. C. Jaeger, *Conduction of Heat in Solids.* Second Edition. Oxford University Press, Oxford, Great Britain, pp. 261-262 (1959).

15. K. Pruess, TOUGH user's guide. *Rep. NUREG/CR-4645*, Nuclear Regulatory Commission, Washington, D.C. (1987).

16. R. C. Schroeder, M. J. O'Sullivan, K. Pruess; R. Celati, and C. Ruffilli, Reinjection studies of vapor-dominated systems. *Geothermics*, **11**(2), 93-119 (1982).

17. A. T. Corey, The interrelation between gas and oil relative permeabilities. *Producers Monthly*, pp. 38-41, November (1954).

18. A. K. Verma, K. Pruess, C. F. Tsang, and P. A. Witherspoon, A study of two-phase concurrent flow of steam and water in an unconsolidated porous medium. In *Heat Transfer in Porous Media and Particulate Flows*, HTD Vol. 46, *Proceedings of the 23rd ASME/AIChE National Heat Transfer Conf.*, Denver, 4-7 August, pp. 135-143 (1985).

19. M. Th. van Genuchten, A closed-form equation for predicting the hydraulic conductivity of unsaturated soils. *Soil Sci. Soc. Am. J.* **44**, 892-898 (1980).

20. Y. W. Tsang and K. Pruess, A study of thermally induced convection near a high-level nuclear waste repository in partially saturated fractured tuff. *Water Resour. Res.* **23**(10), 1958-1966 (1987).

21. P. A. Witherspoon, N. G. W. Cook, and J. E. Gale, Progress with field investigations at Stripa. *Rep. LBL-10559 (SAC-27)*, Lawrence Berkeley Laboratory, Berkeley, Calif. (1980).

22. I. Javandel and P. A. Witherspoon, Thermal analysis of the stripa heater test data from the full scale drift. *Rep. LBL-13217 (SAC-43)*, Lawrence Berkeley Laboratory, Berkeley, Calif. (1981).

23. A. Verma and K. Pruess, Thermohydrological conditions and silica redistribution near high-level nuclear wastes emplaced in saturated geological formations. *J. Geophys. Res.* **93**(B2), 1159-1173 (1988).

24. L. H. Baetslé, A. Bonne, P. Henrion, M. Put, and J. Patyn, Assessment of the combined effects of temperature increase, water convection, migration of radionuclides, and radiolysis on the safety of a nuclear waste repository in the boom clay. In *Coupled processes associated with nuclear waste repositories*, C. F. Tsang, ed., Academic Press, Orlando, Florida, pp. 225-236 (1987).

25. International Formulation Committee, *A formulation of the thermodynamic properties of ordinary water substance.* IFC Secretariat, Düsseldorf, Germany (1967).

Appendix A: Thermophysical Properties

The constitutive relationships used to define the thermodynamic parameters in terms of the primary variables are taken from the numerical model TOUGH [15], described in Section 5.

Steam tables, given by the International Formulation Committee [25], provide closed-form expressions for ρ, u , h , μ, and σ (used in P_c) as functions of P and T .

Relative permeabilities k_{rl} and k_{rg} and capillary pressure P_c are functions of liquid and gas saturation S_l and S_g ; examples are shown in Table 1 and Table 4. Thermal conductivity κ also varies with liquid saturation, as given by [9, 10]

$$\kappa = \kappa_g + \sqrt{S_l}(\kappa_l - \kappa_g) \tag{A1}$$

where κ_g and κ_l are the values of thermal conductivity for dry and liquid-saturated rock, respectively.

Porosity depends on pressure and temperature

$$\phi = \phi_0 \exp\left[\beta_r (P - P_0) + \alpha_r (T - T_0)\right] \tag{A2}$$

where β_r and α_r are constant rock compressibility and rock expansivity, respectively, and ϕ_0 is the value of porosity for $P_g = P_0$ and $T = T_0$.

Intrinsic permeability k , rock density ρ_r , and rock specific heat c_r are assumed to be constants. The relationships needed for two-component systems including air are not included here, but may be found in the description of TOUGH [15].

Table 1. Material properties, characteristic curves, and boundary conditions used for the similarity-solution results shown in Figures 3 and 4.

Material Properties		
intrinsic permeability	k	$1.\times10^{-13}$ m^2
initial porosity	ϕ_0	0.40
rock compressibility	β_r	$1.\times10^{-7}$ Pa^{-1}
rock expansivity	α_r	0 K^{-1}
rock density	ρ_r	2580 kg/m^3
rock specific heat	c_r	840 J/kg K
thermal conductivity [9, 10]		
liquid-saturated rock	κ_l	1.13 W/m K
gas-saturated rock	κ_g	0.582 W/m K
Characteristic Curves		
relative permeability [11, 12]		
liquid	k_{rl}	$S_l{}^3$
vapor	k_{rg}	$S_g{}^3$
capillary pressure [13]	P_c	$-\sigma(T)\sqrt{\frac{\phi}{k}}f$
		$f = 1.417S_g - 2.12S_g{}^2 + 1.263S_g{}^3$
Boundary Conditions		
$z \rightarrow -\infty$	Q_{w0}	0
	Q_{e0}	200 W/m
$z \rightarrow \infty$	P_0	101325 Pa
	T_0	26 °C

Table 2. Details of the shooting method for the results shown in Figure 3.

Shot	Increment	P_L (MPa)	T_L (°C)	P_U (MPa)	T_U (°C)
1	–	0.10133	360.00	0.05088	45.62
	δP_L	0.10033	360.00	0.04982	45.23
	δT_L	0.10133	354.00	0.05090	42.76
2	–	0.14864	279.86	0.10064	22.11
	δP_L	0.14764	279.86	0.09960	21.82
	δT_L	0.14864	273.86	0.10065	19.07
3	–	0.14929	287.19	0.10133	25.99
			Converged		

Increments: δP_L =–0.001 MPa, δT_L =–6.0 °C (Comparable results are obtained for increment values in the range $10^{-6} < |\delta P_L| < 0.02$ and $0.006 < |\delta T_L| < 24$.)

Accuracy: γ=0.01

Table 3. Material properties, characteristic curves, and mesh spacing used for the TOUGH simulation.

Material Properties		
intrinsic permeability	k	$1.\times10^{-15}$ m^2
initial porosity	ϕ_0	0.40
rock compressibility	β_r	$1.\times10^{-8}$ Pa^{-1}
rock expansivity	α_r	0 K^{-1}
rock density	ρ_r	2600 kg/m^3
rock specific heat	c_r	700 J/kg K
thermal conductivity [9, 10]		
liquid-saturated rock	κ_l	1.13 W/m K
gas-saturated rock	κ_g	0.582 W/m K
Characteristic Curves		
relative permeability		
liquid	k_{rl}	S_l
vapor	k_{rg}	S_g
capillary pressure [13]	P_c	$-\sigma(T)\sqrt{\frac{\phi}{k}}f$
		$f = 1.417S_g - 2.12S_g^2 + 1.263S_g^3$
Mesh Spacing		
Element	Size	Comments
1	Δr_1=0.016 m	Contains 200 W/m heat source
2	Δr_2=0.010 m	
i, i =3,90	$\Delta r_i = a\,\Delta r_{i-1}$	a =1.138
		Center of element 90 is 6755 m, P_g and T are held fixed there.

Table 4. Relative permeability functions shown in Figure 8a.

Function	k_{rl}	k_{rg}
Linear	S_l^*	$1-S_l^*$
Verma et al. [18]	S_l^{*3}	$1.259-1.7615S_l^*+0.5089S_l^{*2}$
Cubic [11, 12]	S_l^{*3}	$(1-S_l^*)^3$
Corey [17]	S_l^{*4}	$(1-S_l^*)^2(1-S_l^{*2})$
van Genuchten [19]	$\sqrt{S_l^*}\left[1-(1-S_l^{*1/\lambda})^\lambda\right]^2$, $\lambda=0.45$	$1-k_{rl}$

Note: S_l^* is reduced liquid saturation, defined in terms of irreducible liquid and gas saturations in various ways for the different relative permeability functions. For the present work, we assume all irreducible saturations to be zero, that is, neither liquid nor gas phase is ever immobile under two-phase conditions, so $S_l^*=S_l$.

Table 5. Values of t_{sat}, the earliest time at which $T = T_{sat}$, for various initial conditions, calculated from equation (44). (Q_{e0}=500 W/m, κ_c =2.2 W/m °C, C_c =2.4 MJ/m^3 °C, r =0.25 m)

	Depth (m)	P_0† (MPa)	T_0‡ (°C)	$T_{sat}(P_0)$ (°C)	t_{sat} (years)
Partially	100	0.1013	13	100	0.117
Saturated	300	0.1013	19	100	0.084
	600	0.1013	28	100	0.051
Fully	300	3	19	234	137
Saturated	600	6	28	276	846
	900	9	37	303	2392
	1200	12	46	325	4722

†Atmospheric pressure for partially saturated cases, hydrostatic for fully saturated cases.
‡∇T =30 °C/km with T =10 °C at zero depth.

Table 6. Values of t_{sat}, the earliest time at which $T=T_{sat}$, for various proposed repository sites, calculated from equation (44) with r=0.25 m.

Geologic Setting (Example Site)	Repository Depth (m)	P_0 (MPa)	T_0 (°C)	$T_{sat}(P_0)$ (°C)	κ_c (W/m°C)	C_c (MJ/m^3°C)	Age of Waste (years)	Q_{e0} (W/m)	t_{sat} (years)
Partially saturated tuff [20] (Yucca Mountain, USA)	348	0.1013	24	100.0	2.3	2.4	8	636[a]	0.029
Granite [21, 22] (Stripa, Sweden)	340	2	10	212.4	3.2	2.1	5	1385	0.21
Basalt [23] (Hanford, USA)	900	9	33	303.3	2.3	2.7	10	691	85
Clay [24] (Mol-Dessel, Belgium)	220	2.2	16	217.2	1.7	2.8	50	300[a]	2456

[a] Not given in reference, estimated from information on areal loading, age of waste, and emplacement configuration.

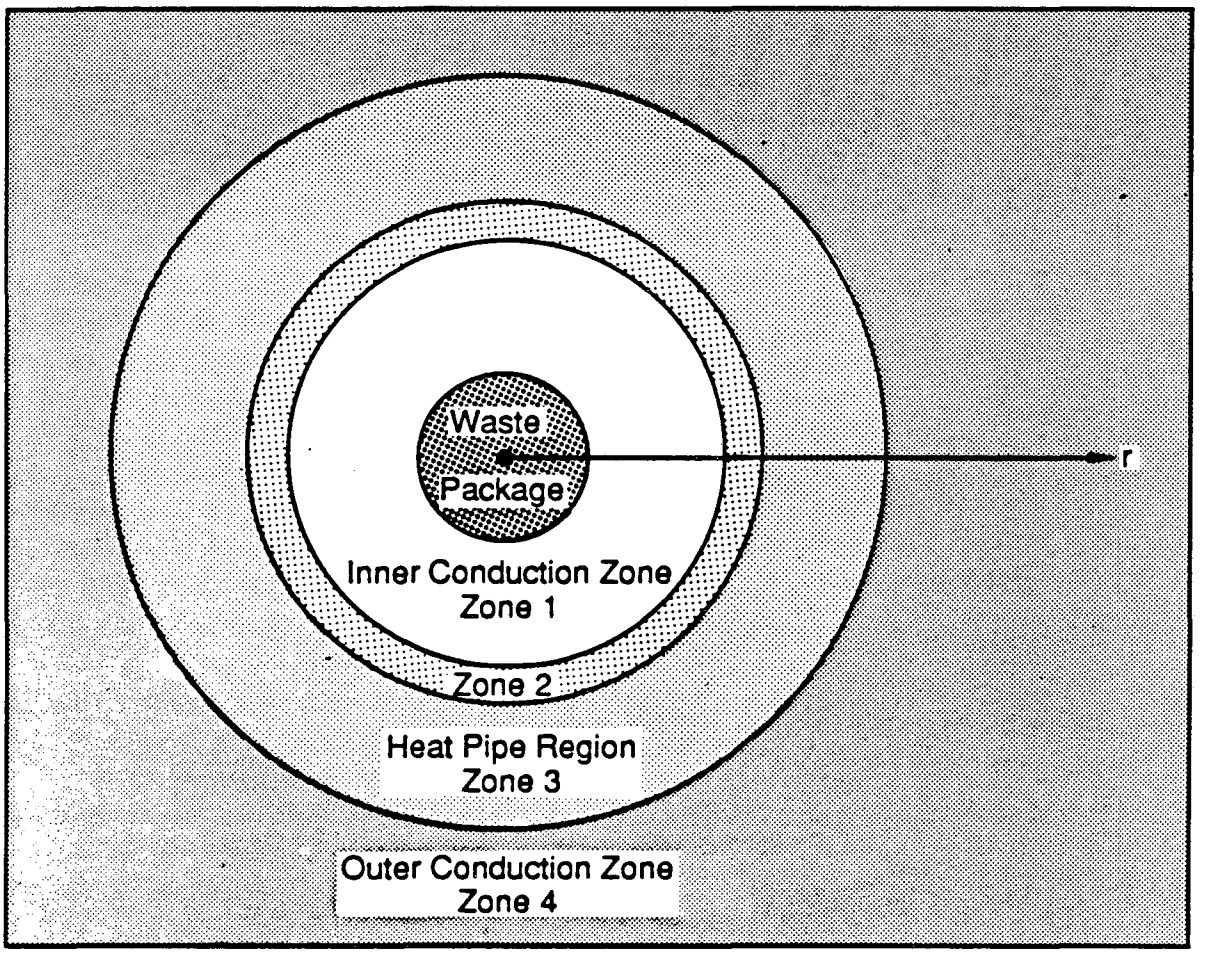

XBL 8611-12738B

Figure 1. Schematic of the conditions achieved at some time after waste emplacement (not to scale). Water is primarily in the liquid phase in zone 4, because $T < T_{sat}$; two-phase conditions prevail in zones 2 and 3, with $T \approx T_{sat}$; fluid in zone 1 is in the gas phase, with $T > T_{sat}$.

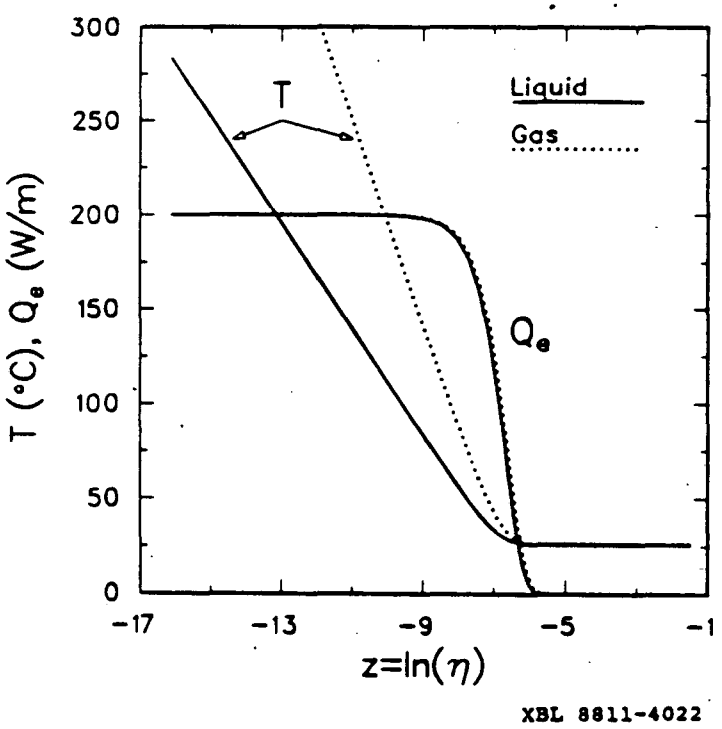

Figure 2. Conduction-only temperature and heat-flow profiles for liquid-saturated and gas-saturated media.

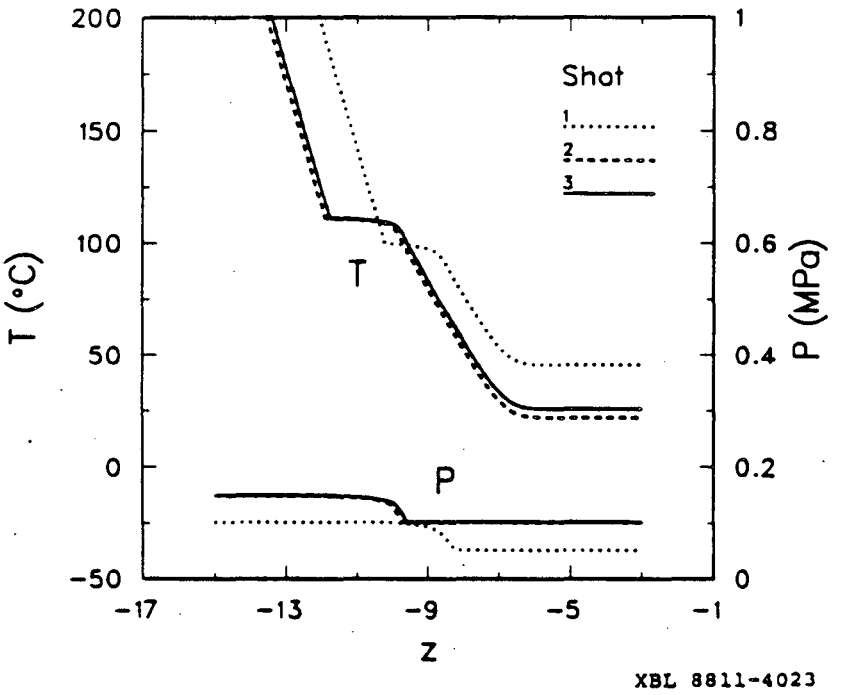

Figure 3. Temperature and pressure profiles illustrating the shooting method.

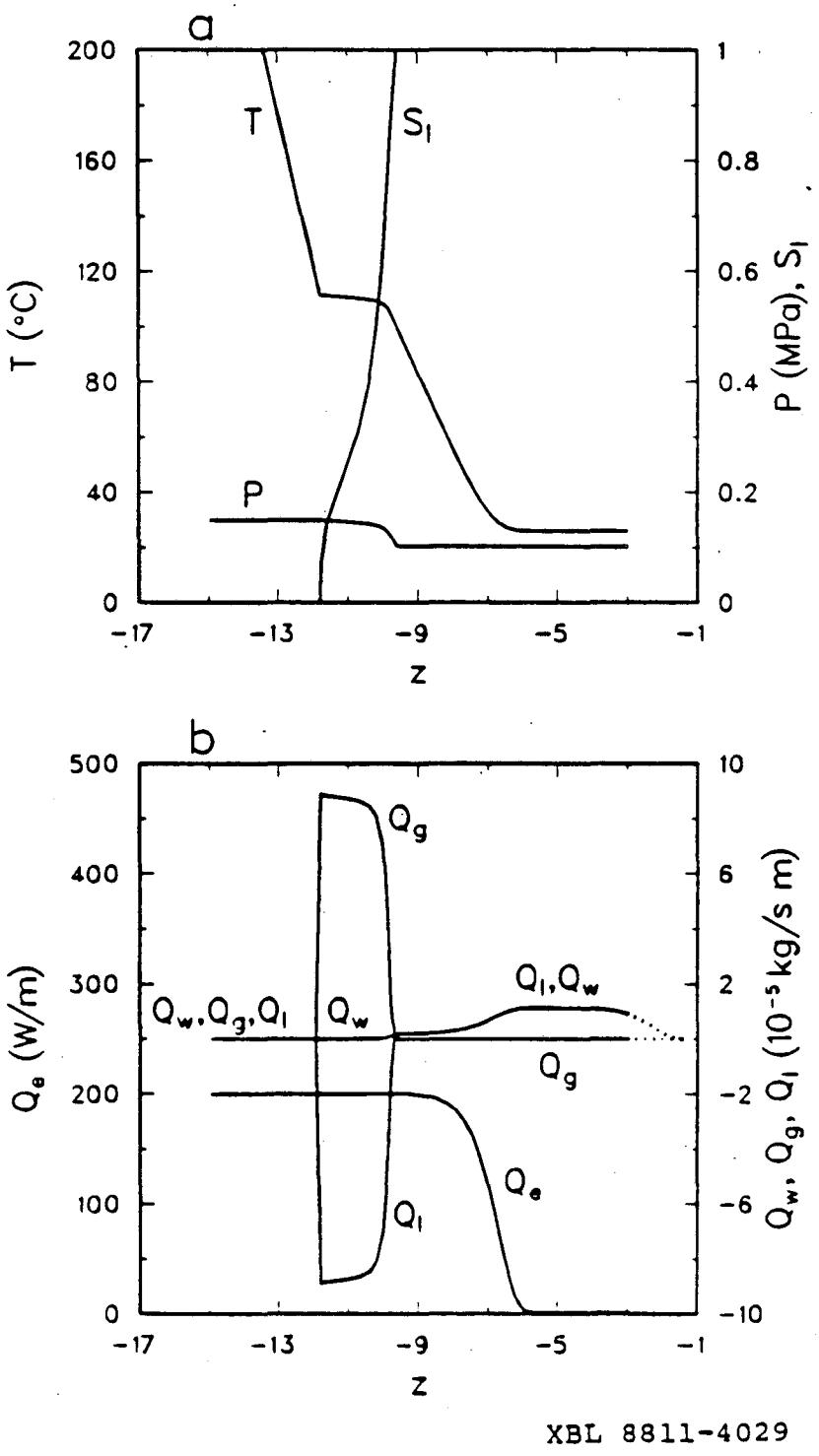

Figure 4. Temperature, pressure, and saturation profiles (4a) and heat, mass, liquid, and gas flow profiles (4b) for the problem described in Table 1.

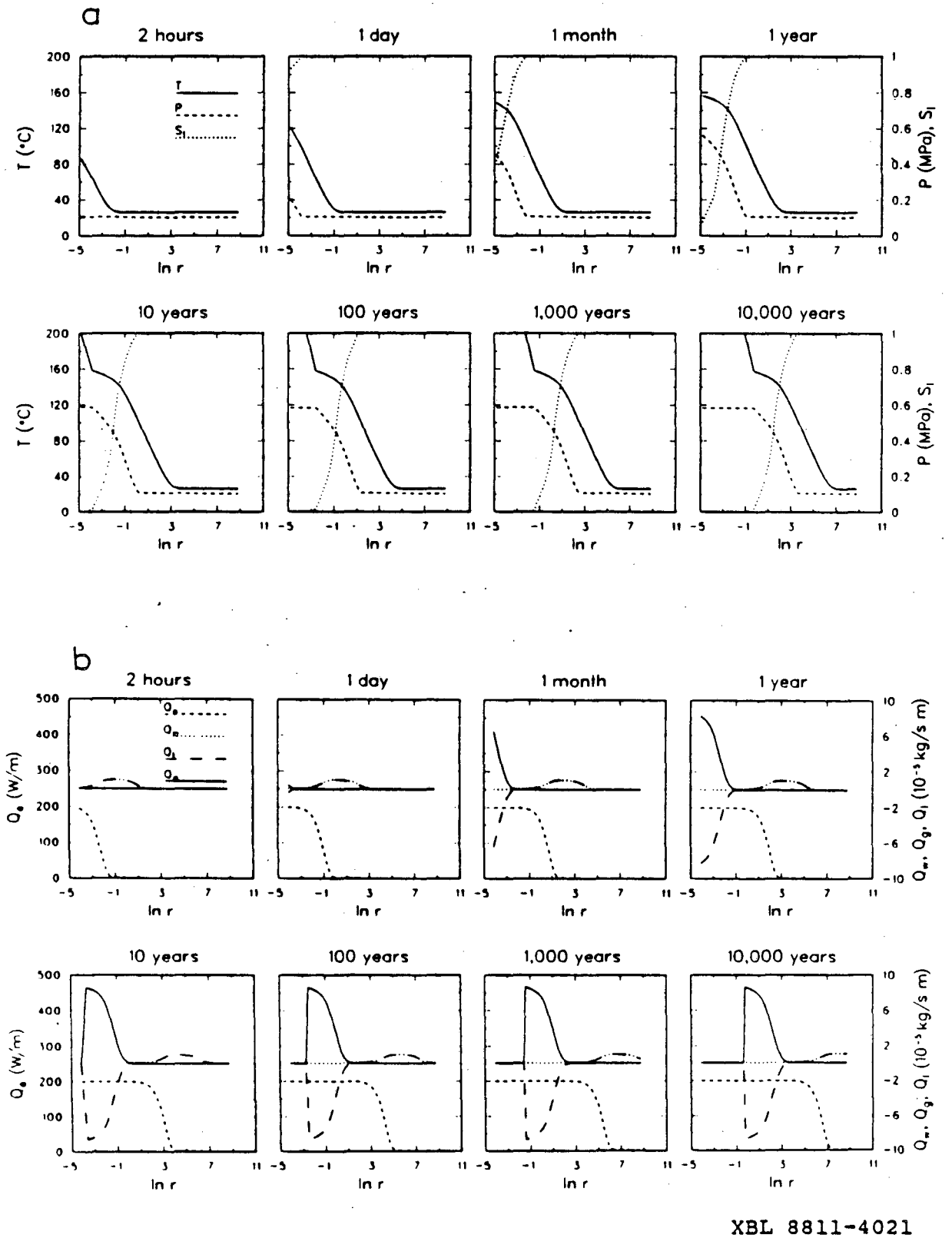

Figure 5. TOUGH simulation for temperature, pressure, and saturation (5a) and heat, mass, liquid, and gas flows (5b) as a function of radial distance for a series of times.

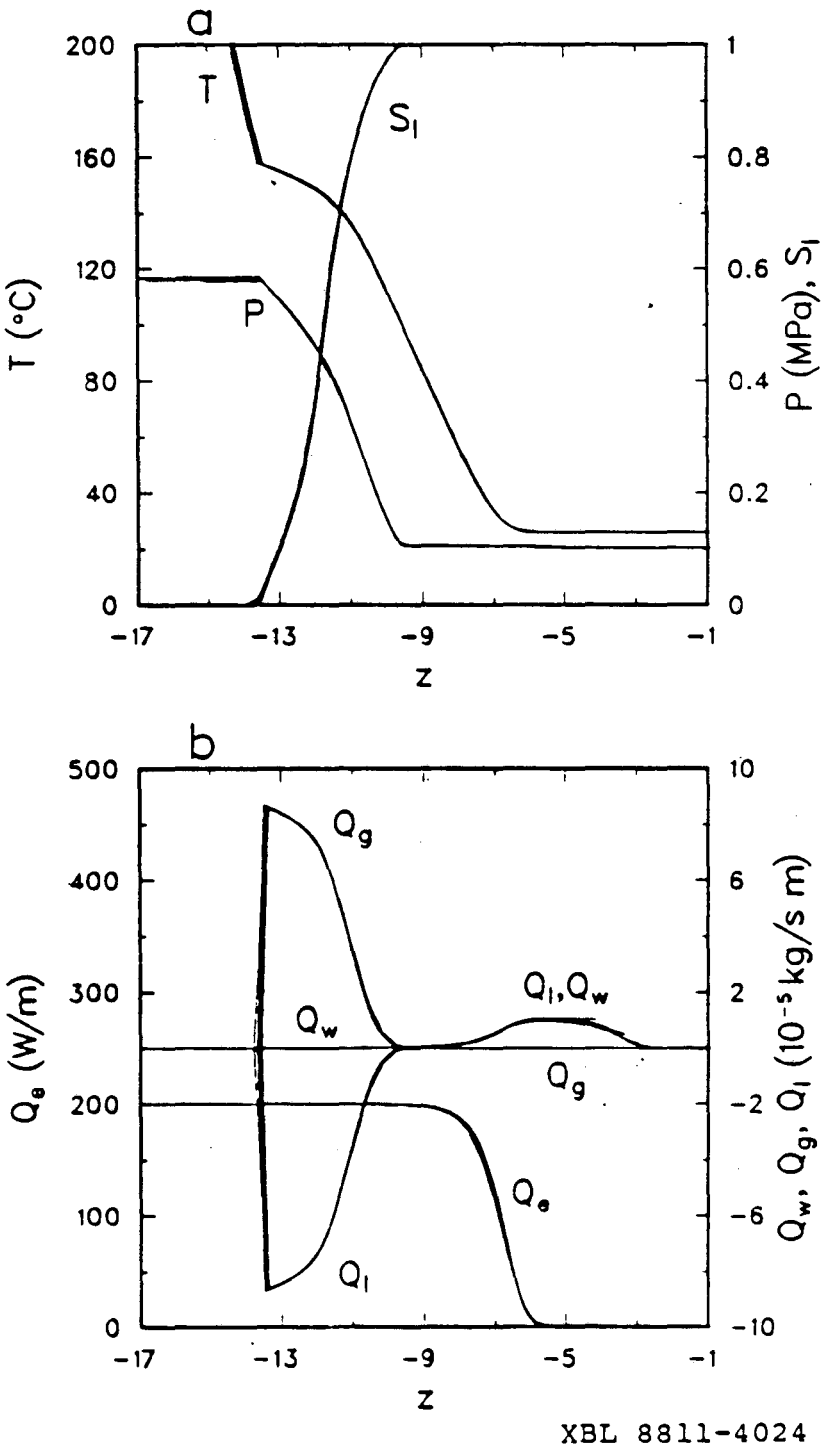

Figure 6. TOUGH simulation for temperature, pressure, and saturation (6a) and heat, mass, liquid, and gas flows (6b) as a function of $z = \ln(r/\sqrt{t})$, with profiles from 21 different times included.

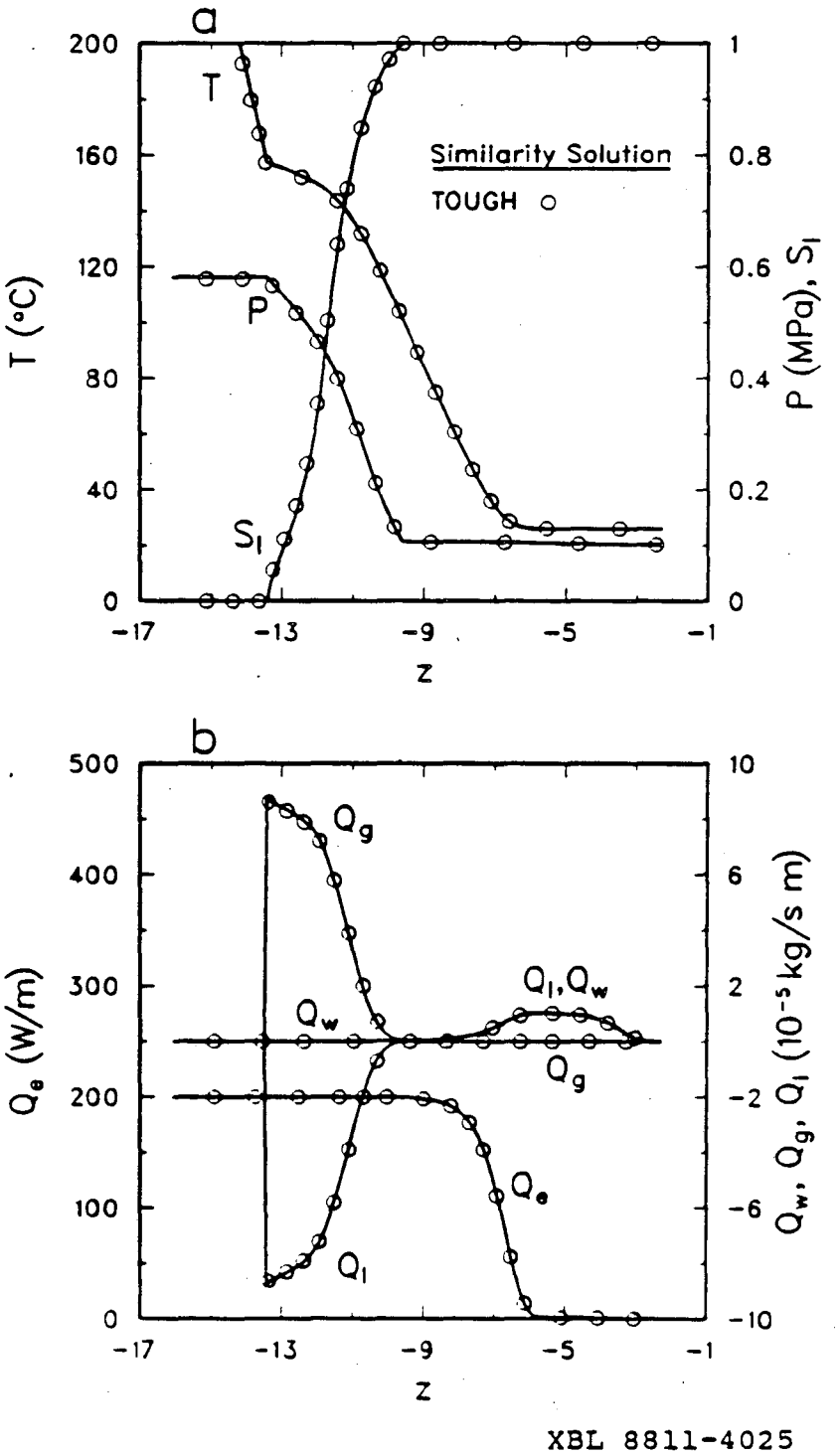

Figure 7. A comparison between the 200-year TOUGH result and the similarity solution for temperature, pressure, and saturation profiles (7a) and heat, mass, liquid, and gas flow profiles (7b).

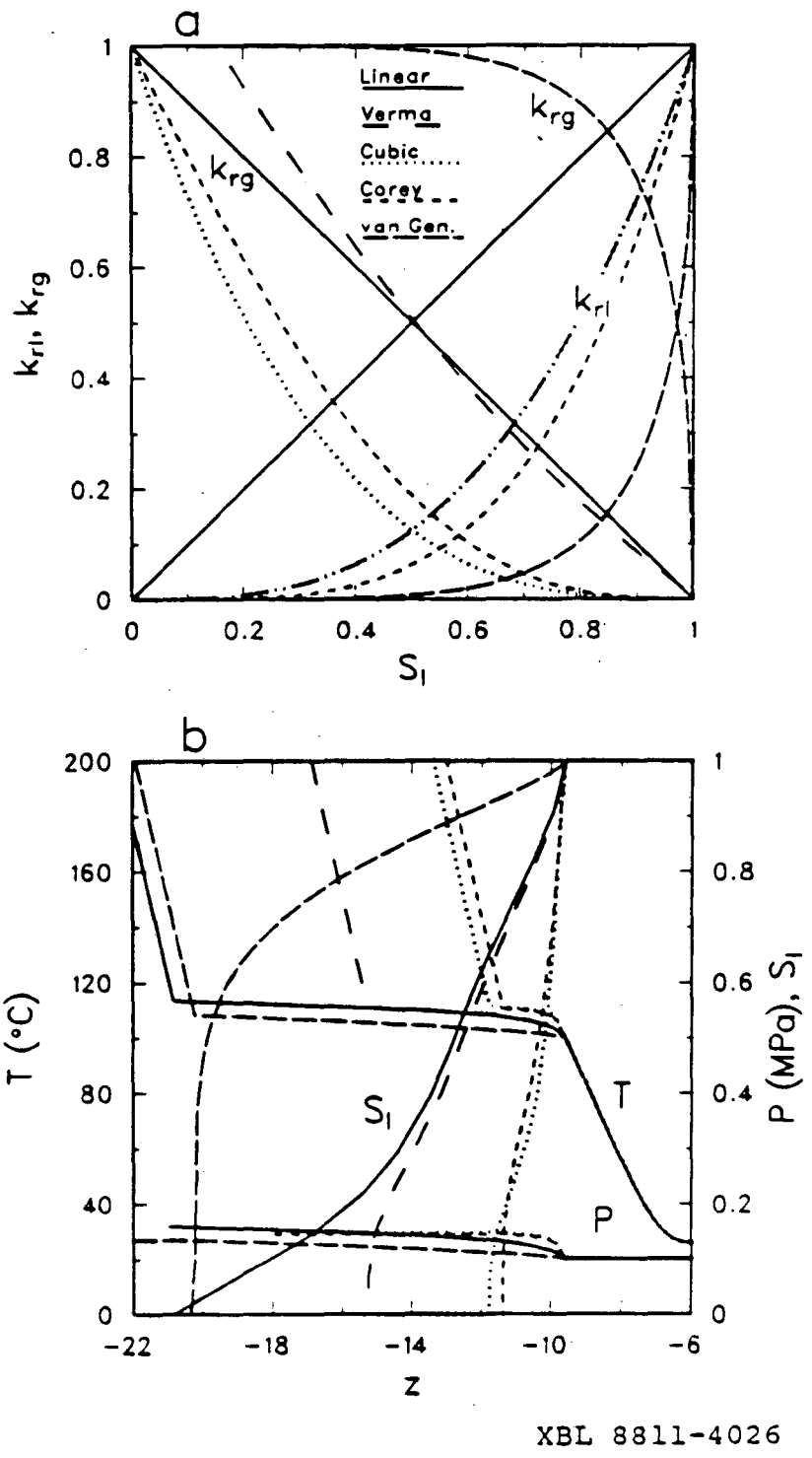

Figure 8. Various relative permeability functions (8a) and the temperature, pressure, and saturation profiles calculated using them (8b). The relative permeability functions are described in Table 4.

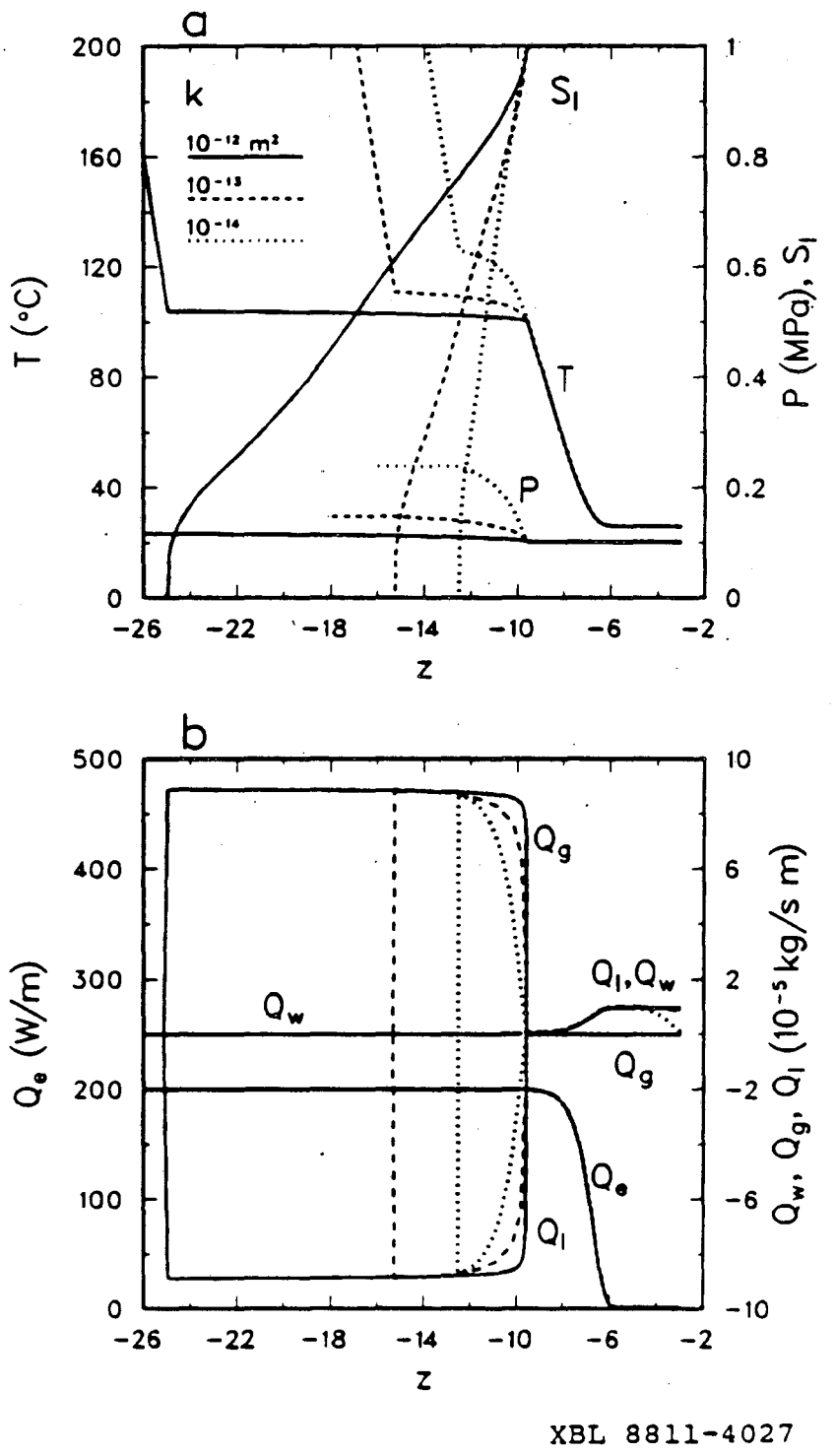

Figure 9. Temperature, pressure, and saturation profiles (9a) and heat, mass, liquid, and gas flow profiles (9b) for several intrinsic permeability values.

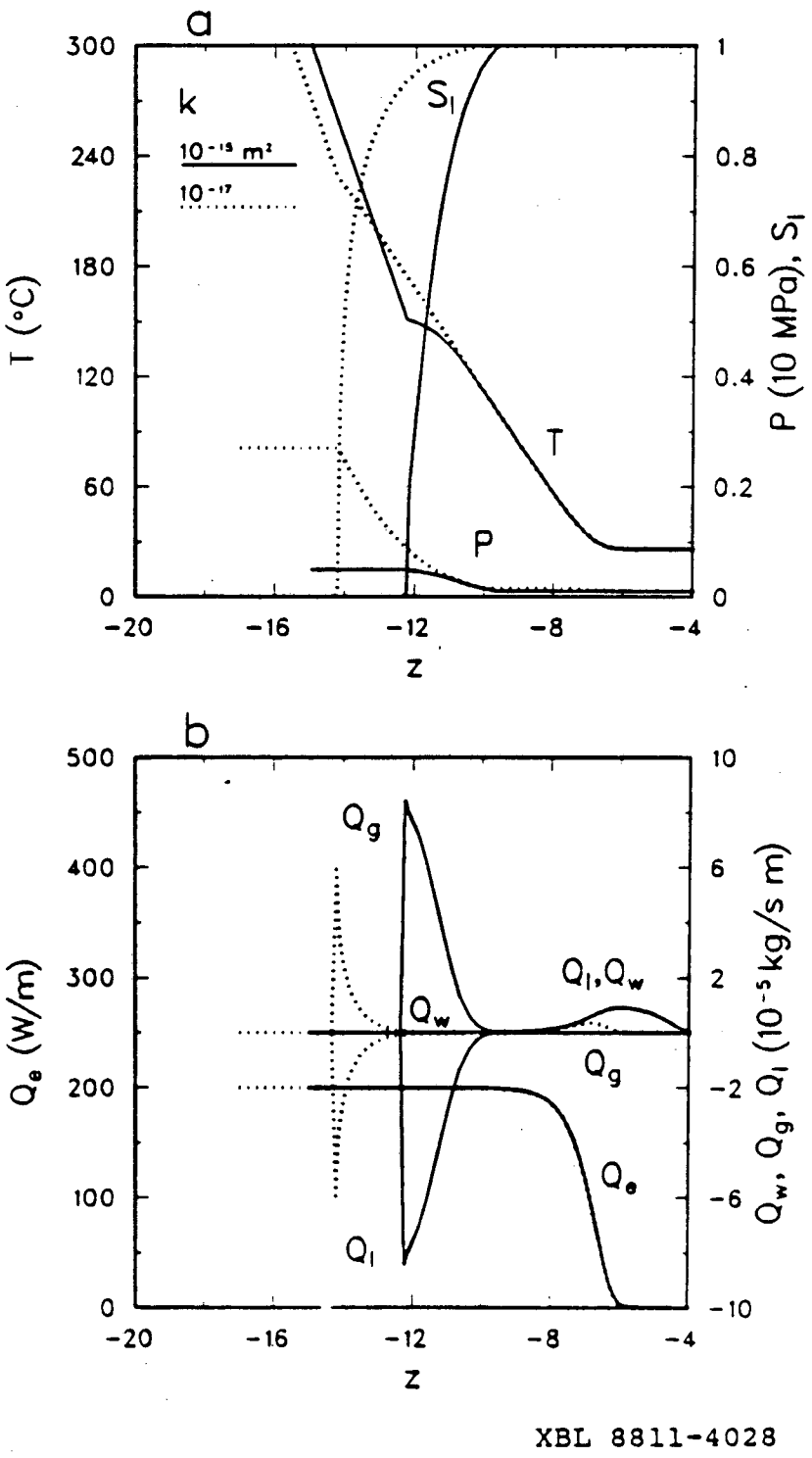

Figure 10. Temperature, pressure, and saturation profiles (10a) and heat, mass, liquid, and gas flow profiles (10b) for low intrinsic permeability values.

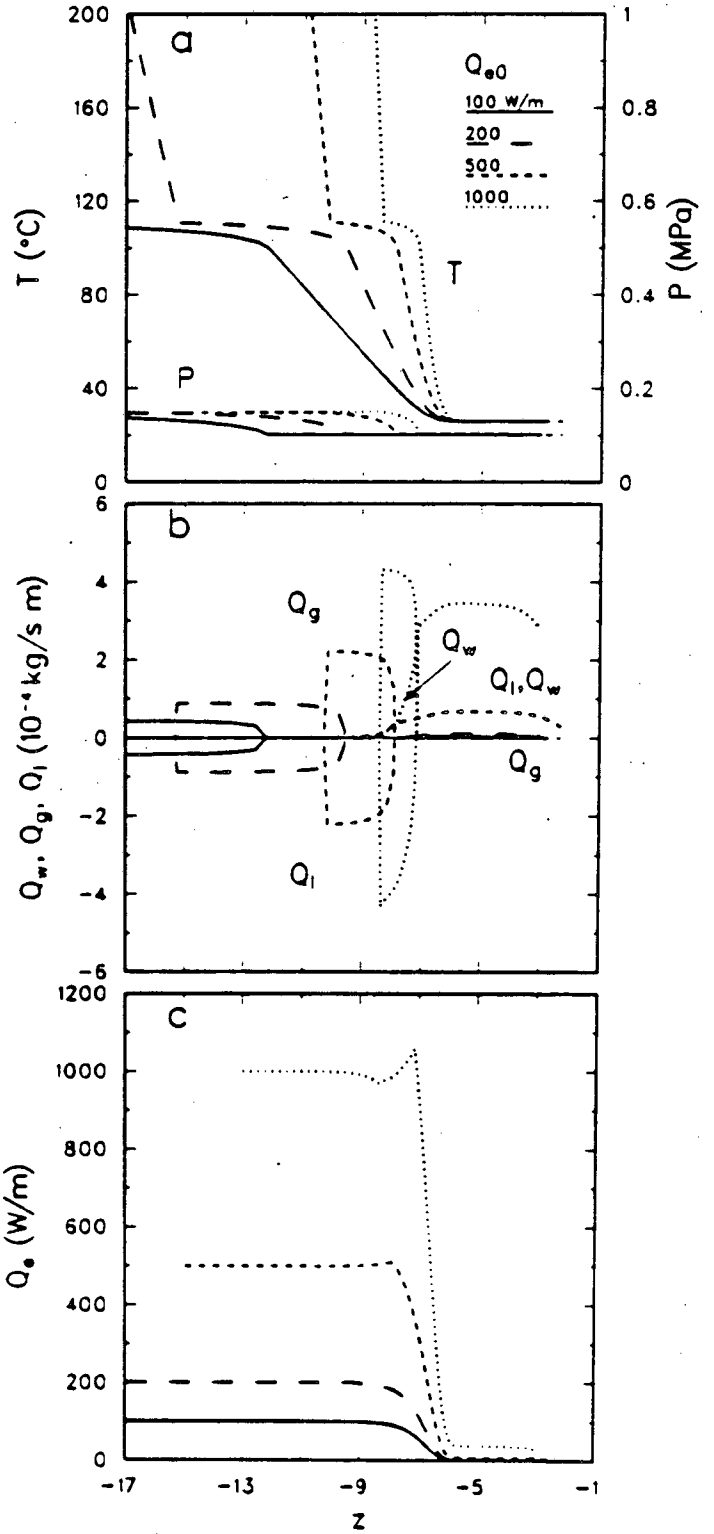

Figure 11. The effect of heat source strength on a) temperature and pressure profiles, b) mass, liquid, and gas flow profiles, and c) heat flow profile.

LAWRENCE BERKELEY LABORATORY
TECHNICAL INFORMATION DEPARTMENT
UNIVERSITY OF CALIFORNIA
BERKELEY, CALIFORNIA 94720